

## MWIR camera calibration for CO<sub>2</sub> quantification

by Vitor F. Paes, Jucélia N. Rosa, Rafael A. M. Ferreira and Matheus P. Porto

Centro Multiusuário de Termografia Científica (CEMTEC) and Graduate Program in Mechanical Engineering, Universidade Federal de Minas Gerais, Brasil. [matheusporto@ufmg.br](mailto:matheusporto@ufmg.br)

### Abstract

This article examines a calibration method for measuring CO<sub>2</sub> concentration with a mid-wave infrared (MWIR) thermal imager equipped with a narrow-band filter. The camera is initially calibrated over a temperature range from 20°C to 80°C using a flat-plate blackbody radiator. From this calibration, a regression equation relating digital counts (C) with radiance (L) is obtained. The accuracy of this regression equation is assessed by comparing the results with expected radiance values. A maximum deviation of 2.78% was observed with an integration time of 3.7 ms. After the calibration process, a spectral-based mathematical model employing the HITRAN Application Programming Interface (HAPI) is used to determine CO<sub>2</sub> concentration in parts per million (ppm) during a person's breathing cycle. Future research will focus on evaluating uncertainties associated with both the calibration regression equation and the application of the mathematical model.

### 1. Introduction

Optical infrared systems are among the most promising techniques for gas sensing due to the strong absorption characteristics of gases in the mid to long wavelength infrared spectra (2.5 μm – 14 μm) [1]. Infrared sensors offer significant advantages over other sensor types, including high sensitivity, selectivity, repeatability, and resolution. Among the various optical gas sensing techniques, thermography stands out as particularly promising. It enables detailed observation of gas dynamics, including the quantification of concentration, spectral emissivity, temperature, and mass flow [2-7].

The accurate measurement of CO<sub>2</sub> concentration using sensing techniques holds significant potential across various scientific domains, including studies to assess patients' breathing capacity [8,9] and quantifying CO<sub>2</sub> emissions from industrial processes [10-12]. Despite its scientific importance, we have not found studies addressing the metrological challenges of utilizing thermography for CO<sub>2</sub> concentration measurement.

This article explores a calibration method for measuring CO<sub>2</sub> concentration using a mid-wave infrared (MWIR) thermal imager equipped with a narrow-band filter. We discuss the challenges of calibrating the camera in-house and applying a line-by-line spectral-based approach for thermography [6,7]. The mathematical model developed for this purpose was implemented in Python and integrated with the HITRAN Application Programming Interface (HAPI) for a robust line-by-line analysis [13-27].

In Section 2, we present the methodology of this work, where a mathematical model is introduced to estimate the radiance absorbed by the detectors. Additionally, we outline the procedure for obtaining the calibration equation of the camera, along with the experimental protocols for camera calibration and CO<sub>2</sub> measurement during a breathing cycle. Then, in Section 3, we present the qualitative results of the calibration process and the post-processed data of the breathing cycle. Finally, Section 4 contains the conclusions drawn from this work.

### 2. Methodology

The methodology of this work is divided into mathematical model, calibration equation of the camera, experimental procedure of calibration, and experimental procedure for the breathing cycle.

#### 2.1 Mathematical model

Figure 1 illustrates the schematic representation of the physical model utilized to estimate the radiance absorbed by the detectors of a thermal imager. The model incorporates thermal radiation components, including blackbody emission (1), emission reflected from the environment and atmosphere, spectral properties of the participating media (2), spectral transmissivity of the lenses (3), spectral transmissivity of the CO<sub>2</sub> filter (4), and spectral responsivity of the detector (5). Equation 1 is used to determine the total thermal radiance absorbed by the detectors, denoted as  $L_{\text{abs}}$ , following the physical model depicted in Figure 1. On the right side of the equation,  $L_{\lambda}(T_{\text{ob}})$ ,  $L_{\lambda}(T_{\text{ref}})$ , and  $L_{\lambda}(T_{\text{atm}})$  represent the spectral radiance emitted by the blackbody, the spectral radiance of the reflected component from the environment, and the spectral radiance from the gases of the atmosphere, respectively. The other terms in the equation include the spectral emissivity of CO<sub>2</sub> ( $\epsilon_{\text{atm},\lambda}$ ), the lens' spectral transmissivity ( $\tau_{\text{lens},\lambda}$ ), the filter's spectral transmissivity ( $\tau_{\text{filter},\lambda}$ ), and the detector's spectral responsivity ( $R_{\lambda}$ ).

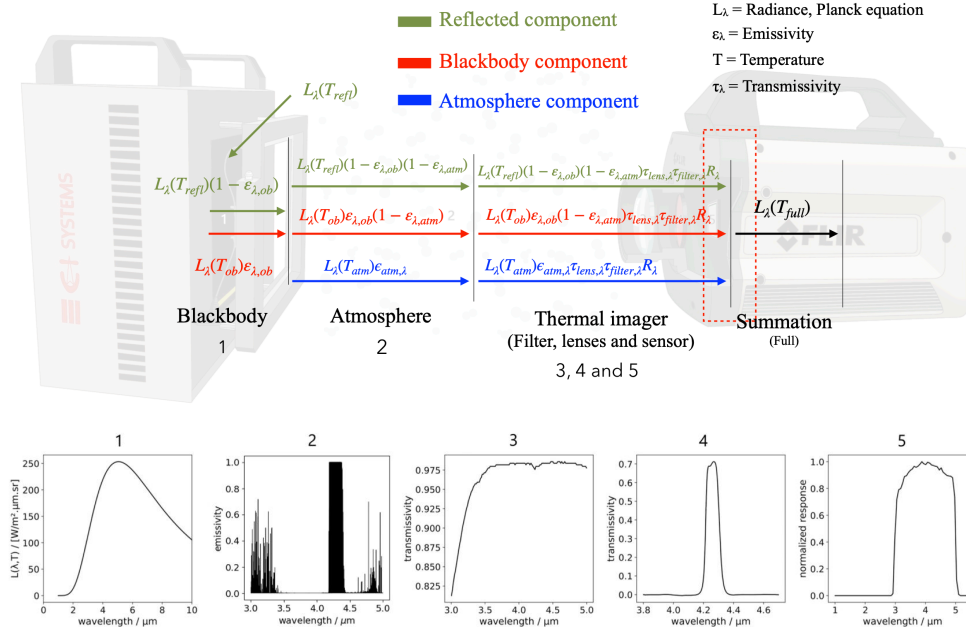


Fig. 1: Physical representation of the calibration process.

$$L_{abs} = \int_{\lambda_1}^{\lambda_2} \left[ L_\lambda(T_{ob})\epsilon_{\lambda,ob}(1 - \epsilon_{atm,\lambda})\tau_{lens,\lambda}\tau_{filter,\lambda}R_\lambda + L_\lambda(T_{refl})(1 - \epsilon_{\lambda,ob})(1 - \epsilon_{atm,\lambda})\tau_{lens,\lambda}\tau_{filter,\lambda}R_\lambda + L_\lambda(T_{atm})\epsilon_{atm,\lambda}\tau_{lens,\lambda}\tau_{filter,\lambda}R_\lambda \right] d\lambda \quad (1)$$

Figure 2 presents simulations for spectral radiance absorbed by detectors,  $L_{\lambda,abs}$ , for various concentrations of  $CO_2$ . In all scenarios, the background is a blackbody maintained at  $50^\circ C$ . The atmospheric line-of-sight is divided into two atmospheric windows. The first window represents a clean atmosphere, with 50% of air humidity, a  $CO_2$  concentration of 1,000 ppm, a temperature of  $22^\circ C$ , a line-of-sight distance of 90 cm, and an atmospheric pressure of 0.935 atm. The second window consists of exhaled gases during a breathing cycle, with a temperature of  $27^\circ C$  and a line-of-sight distance of 30 cm.

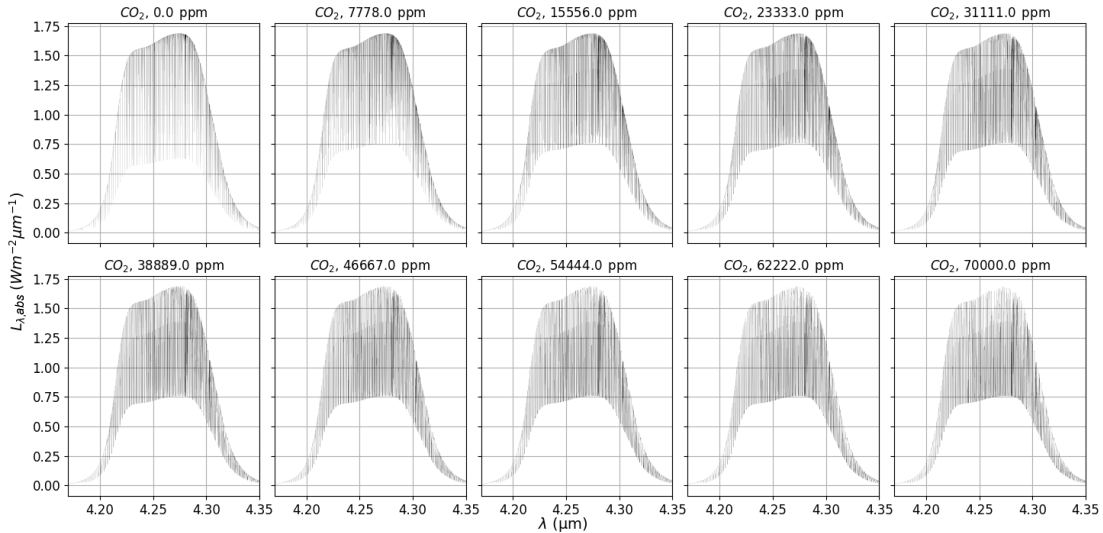
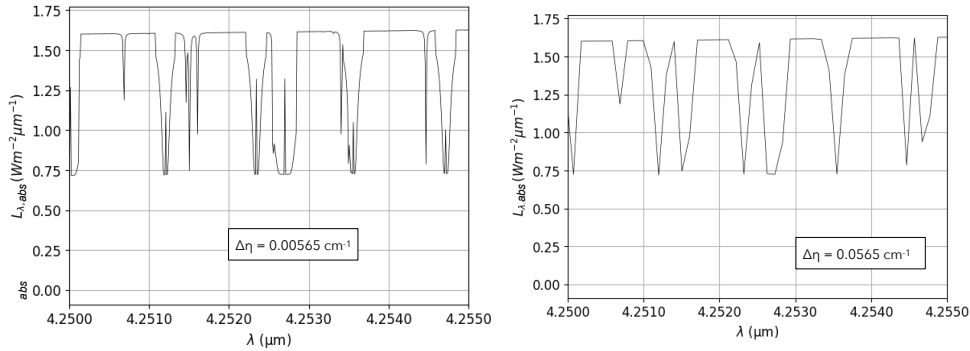


Fig. 2: Simulations of  $L_{\lambda,abs}$  for different  $CO_2$  concentrations. Value of 0 ppm in the first graph indicates absence of  $CO_2$  emissions from other sources than from the atmosphere.

Figure 3 displays the results of the HAPI simulation, showing CO<sub>2</sub> spectra at a concentration of 23,333 ppm. The spectra cover a narrow band from 4.25 to 4.255 μm and are presented at two different spectral resolutions.



**Fig. 3:** Changes in  $L_{\lambda,abs}$  for different spectral resolutions.

### 2.2 Calibration equation of the camera

The camera calibration equation is derived through six sequential steps: setting the blackbody to a temperature denoted as  $T_{ob}$ ; measurement of atmospheric temperature, humidity, and CO<sub>2</sub> concentration; estimation of the radiance reaching the detectors using Equation 1; recording a digital count,  $C$ , from the thermal imager; plotting graphs of  $C$  versus  $L_{abs}$ ; deriving a regression equation of  $L_{abs}$  as a function of  $C$ , constituting the camera's calibration equation.

Equation 2 presents the regression relation used as the camera calibration equation. Radiance values,  $L_{abs}$ , are related to the digital number of counts  $C$ , where  $a$  and  $b$  are obtained by regression analysis.

$$L_{abs} = \frac{C - a}{b} \tag{2}$$

The number of counts,  $C$ , in Equation 2, needs correction due to the increasing internal temperature of the thermal imager. Equation 3 is utilized to derive a corrected number of counts ( $C$ ) from the counts extracted from the camera, denoted as  $C(T_{int})$ . The corrected counts,  $C$ , depend on the temperature coefficient ( $K_{temp}$ ), the reference temperature ( $T_{ref}$ ) - defined as the initial recorded internal temperature value - and the current internal temperature ( $T_{int}$ ). The coefficient  $K_{temp}$  must be determined from a previous experiment using regression analysis.

$$C = C(T_{int}) + K_{temp}(T_{ref} - T_{int}) \tag{3}$$

The steps outlined for utilizing the camera's calibration equation are as follows: pointing the camera towards a gas; measuring the background radiance or temperature; measuring atmospheric temperature, humidity, and the atmospheric gases' concentration; recording a digital count,  $C$ ; employing the calibration equation to obtain  $L_{abs}$ ; and utilizing Equation 1 to determine CO<sub>2</sub> concentration.

### 2.3 Experimental procedure of calibration

Figure 4 shows a picture of the calibration procedure of the camera. We used a Flir x6801 MWIR thermal imager, a CI SYSTEMS SR800-N flat plate radiator, with an estimated emissivity of 0.98, and a narrow band filter from Spectrogon, with center wavelength of  $4,285\text{nm} \pm 20 \text{ nm}$  and a half-width length of  $80 \pm 15 \text{ nm}$ . Additionally, a Testo 410 thermo-hygrometer was used to measure the ambient temperature, CO<sub>2</sub> concentration, and relative humidity.



**Fig. 4.** Calibration setup for the MWIR camera equipped with a spectral filter.

Table 1 outlines the experimental conditions for calibration. The thermal imager was positioned in front of the flat plate radiator at a distance of 0.8 m, ensuring simultaneous calibration of most pixels. For each calibration point, blackbody temperature, ambient temperature, humidity, concentration of CO<sub>2</sub>, atmospheric pressure, and digital counts from the thermal imager were recorded with an integration time of 3.7 ms. A temperature range of 20°C to 80°C was utilized as the source for deriving the camera's regression equation, with four intermediate temperature points (25°C to 75°C) for qualitative assessment of calibration performance.

**Table 1. Experimental conditions for the calibration of the camera.**

| T <sub>ob</sub> (°C) | T <sub>amb</sub> (°C) | Humidity (%) | CO <sub>2</sub> (ppm) | P <sub>amb</sub> (Pa) | Data set    |
|----------------------|-----------------------|--------------|-----------------------|-----------------------|-------------|
| 20                   | 22.4                  | 56.3         | 675                   |                       |             |
| 30                   | 22.6                  | 56.8         | 679                   |                       |             |
| 40                   | 22.7                  | 51.3         | 697                   |                       |             |
| 50                   | 22.5                  | 52.7         | 708                   | 92,640                | Calibration |
| 60                   | 22.8                  | 56.2         | 724                   |                       |             |
| 70                   | 22.8                  | 51           | 727                   |                       |             |
| 80                   | 22.4                  | 48.3         | 733                   |                       |             |
| 75                   | 22.7                  | 54.4         | 736                   |                       |             |
| 65                   | 22.8                  | 51.4         | 755                   | 92,640                | Validation  |
| 35                   | 22.5                  | 51           | 764                   |                       |             |
| 25                   | 22.8                  | 53.4         | 789                   |                       |             |

#### 2.4 Experimental procedure for the breathing cycle

The next section presents measurements of CO<sub>2</sub> concentration throughout a breathing cycle under controlled conditions. Figure 5 displays the results captured using the MWIR camera with a narrow band filter taken during the inhalation and exhalation phases.

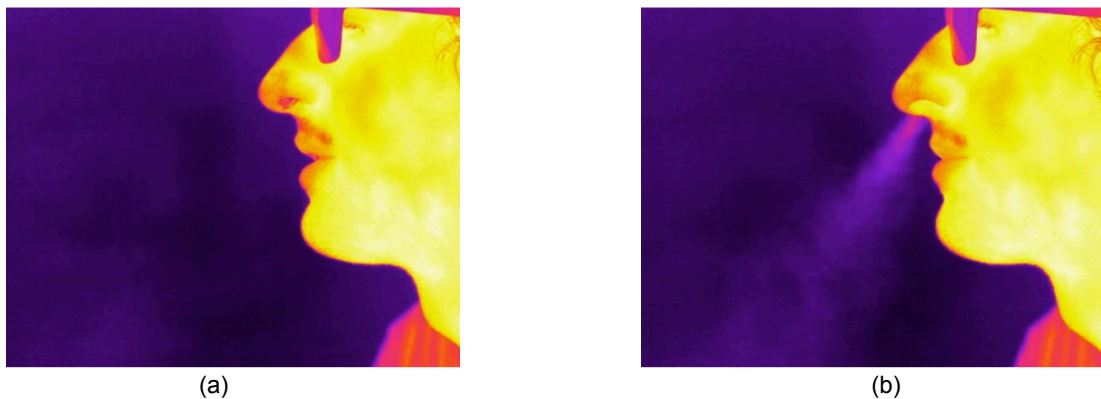


**Fig. 5. Breathing process using the MWIR camera with a CO<sub>2</sub> filter: (a) inhaling process, and (b) exhaling process.**

### 3. Results and discussion

Figure 6 presents the experimental results of calibration. Values of the coefficients, obtained for Equations 2 and 3, are listed in Table 2.

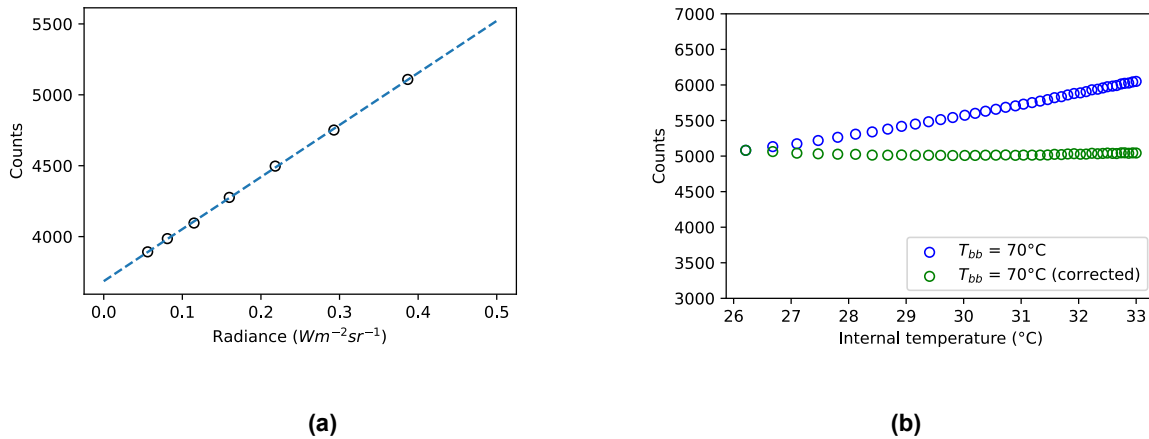


**Fig. 6** Experimental results of the calibration procedure: (a) corrected number of counts  $C$  as a function of radiance, and (b) the extracted number of counts  $C(T_{int})$  in blue, alongside the corrected number of counts ( $C$ ) in green.

**Tab. 2.** Coefficients of the camera calibration.

| $K_{temp}$ | $T_{ref}$ | a       | b       |
|------------|-----------|---------|---------|
| 153.5      | 26.2      | 3672.02 | 3685.74 |

Results of the calibration performance are presented in Table 3. We compare the radiance estimated using Equation 1 with the radiance values obtained from Equations 2 and 3 and provide the absolute percentage deviation (%). Notably, some values of percentage deviation from the validation data set are lower than those from the calibration data set, which was used to develop the regression equation.

**Tab. 3.** Results of the camera calibration for radiance as a function of digital counts.

| Set point [°C] | Radiance from the mathematical model ( $W\ m^{-2}\ sr^{-1}$ ) — Equation 1 | Radiance from calibration equation ( $W\ m^{-2}\ sr^{-1}$ ) — Equations 2 and 3 | Absolute percentage deviation (%) | Data set    |
|----------------|--|---|-----------------------------------|-------------|
| 20             | 0.05586  | 0.05630   | 0.79                              | Calibration |
| 30             | 0.08093  | 0.08172   | 0.97                              |             |
| 40             | 0.11484  | 0.11164   | 2.78                              |             |
| 50             | 0.15975  | 0.16088   | 0.71                              |             |
| 60             | 0.21818  | 0.22096   | 1.27                              |             |
| 70             | 0.29284  | 0.29024   | 0.89                              |             |
| 80             | 0.38678  | 0.38744   | 0.17                              |             |
| 25             | 0.06744  | 0.06833   | 1.32                              | Validation  |
| 35             | 0.09664  | 0.09671   | 0.07                              |             |
| 65             | 0.25330  | 0.25064   | 1.05                              |             |
| 75             | 0.33721  | 0.34144   | 1.24                              |             |

We conducted a measurement where an individual stood in front of a blackbody, allowing us to measure the  $CO_2$  exhaled through the nose during the breathing process. This demonstration serves to illustrate the capabilities of our methodology. In Figure 7, we showcase the outcomes of a post-processing routine developed in Python. Figure 7(a) displays the radiance values in  $W\ m^{-2}\ sr^{-1}$ , while Figure 7(b) depicts  $CO_2$  concentrations in parts per million (ppm) for a line-of-sight distance of 30 cm. Notably, the  $CO_2$  concentration exceeds 60,000 ppm at the End-Tidal Carbon Dioxide (ETCO<sub>2</sub>) point. This observation could be attributed to the individual remaining stationary in a confined space for a long time [28].

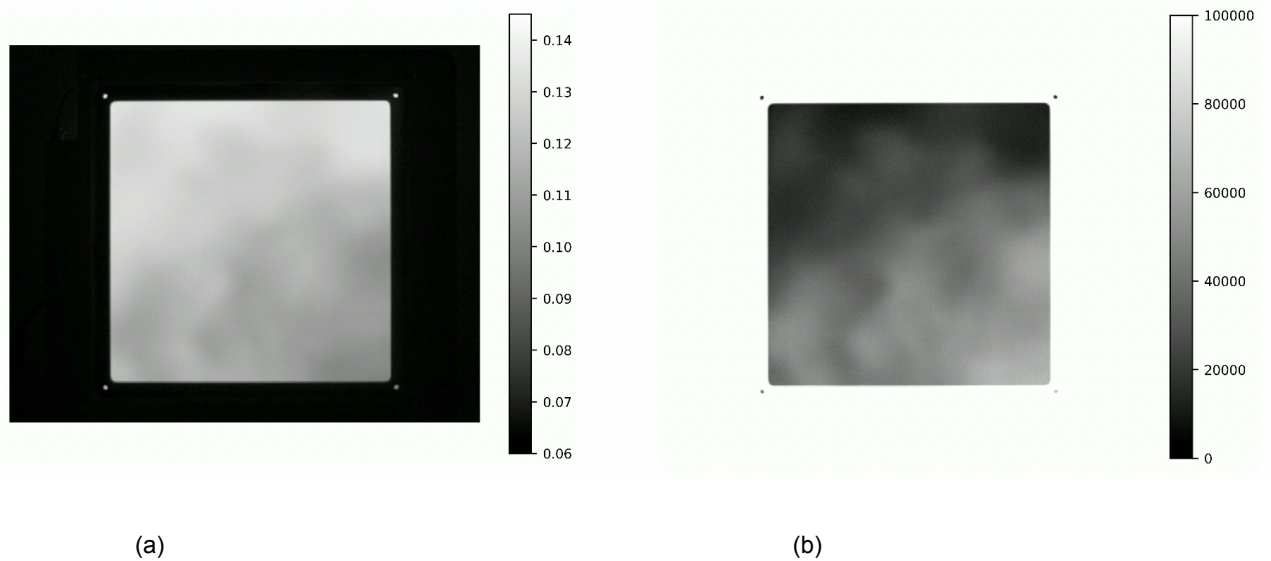


**Fig. 7:** Post-processed thermography during a breathing cycle. (a) radiance, in  $W m^{-2} sr^{-1}$ ; (b) ppm of  $CO_2$ , for a line-of-sight 30 cm.

#### 4. Conclusion

In this study, we explore the calibration method for measuring  $CO_2$  levels using a mid-wave infrared (MWIR) camera equipped with a narrow-band filter. We developed a calibration equation for the camera by calibrating it against a blackbody source. This equation allows us to convert the digital counts captured by the camera into spectral radiance. Using a mathematical model based on spectral analysis, we then estimate  $CO_2$  concentrations from these radiance values.

To evaluate the calibration process, we performed qualitative tests at intermediate points, finding deviations similar to those observed at the original calibration points. Future research should further investigate the impact of integration time on the calibration.

Additionally, we measured the dynamics of  $CO_2$  concentration during a breathing cycle, detecting peaks over 60,000 parts per million (ppm) at the end-tidal  $CO_2$  (ETCO<sub>2</sub>) level, considering a line-of-sight distance of 30 cm. Estimating the uncertainty associated with these measurements is essential for future studies.

#### Acknowledgements

Authors would like to thank the financial support from FAPEMIG (Fundação de Amparo à Pesquisa do Estado de Minas Gerais), also CNPq - Conselho Nacional de Desenvolvimento Científico e Tecnológico, Coordenação de Aperfeiçoamento de Pessoal de Nível Superior - Brasil (CAPES) - Finance Code 001.

#### References

- [1] JHA, R. K., 2021, Non-dispersive infrared gas sensing technology: A review. **IEEE Sensors Journal**, Vol. 22.
- [2] BLUNCK, D. L., 2022, Review: Applications of infrared thermography for studying flows with participating media, **Experimental Thermal and Fluid Science**, Volume 130.
- [3] NARAYANAN, V., PAGE, R.H. & SEYED-YAGOOBI, J., 2003, Visualization of air flow using infrared thermography. **Experiments in Fluids** 34, 275–284.
- [4] CHUAH, K. H., SAITO, K., HASHIBA, Y., GOTODA, H., WILLIAMS, F. A., 2016. A Spectrally Resolved Imaging Method for Investigating Alcohol Pool Fires. **Combustion Science and Technology**, 188(2).
- [5] NEWALE, A. S., RANKIN, B. A., LALIT, H. U., GORE, J. P., MCDERMOTT, R. J., 2015, Quantitative infrared imaging of impinging turbulent buoyant diffusion flames, **Proceedings of the Combustion Institute**, Volume 35.
- [6] FERREIRA, R.A.M., POTTIE, D.L.F., DIAS, L.H.C., BRAZ, J.F.C., PORTO, M.P., 2019, A directional-spectral approach to estimate temperature of outdoor PV panels, **Solar Energy**, Vol. 183.

[7] MOREIRA, M.O., ABRÃO, A.M., FERREIRA, R.A.M., PORTO, M.P., 2021, Temperature monitoring of milling processes using a directional-spectral thermal radiation heat transfer formulation and thermography, **International Journal of Heat and Mass Transfer**, Vol. 171.

Got it, here they are:

[8] TELSON, Y. C., FURLAN, R. M. M., PORTO, M. P., FERREIRA, R. A. M., & MOTTA, A. R., 2023. Evaluation of the breathing mode by infrared thermography. **Brazilian Journal of Otorhinolaryngology** (English Edition), 89(6).

[9] TELSON, Y. C., FURLAN, R. M. M., PORTO, M. P., FERREIRA, R. A. M., & MOTTA, A. R., 2024. **CoDAS**, vol. 36.

[10] SALAMAH, U., SAKTI, S. P., SOETEDJO H., NABA A., 2022, Non-contact technique for CO<sub>2</sub> gas monitoring using thermal imaging camera. **J. Phys.: Conf. Ser.** 2165 012019.

[11] JOHNSON, J., SHAW, J., LAWRENCE, R., NUGENT, P., DOBECK, L., SPANGLER, L., 2012, Long-wave infrared imaging of vegetation for detecting leaking CO<sub>2</sub> gas. **Journal of Applied Remote Sensing**, 6(1).

[12] D. M. TRATT et al., 2017, MAHI: An Airborne Mid-Infrared Imaging Spectrometer for Industrial Emissions Monitoring, **IEEE Transactions on Geoscience and Remote Sensing**, vol. 55.

[13] GORDON, I.E., ROTHMAN, L.S., HARGREAVES, R.J., HASHEMI, R., KARLOVETS, E.V., SKINNER, F.M., CONWAY, E.K., HILL, C., KOCHANOV, R.V., TAN, Y., WCISŁO, P., FINENKO, A.A., NELSON, K., BERNATH, P.F., BIRK, M., BOUDON, V., CAMPARGUE, A., CHANCE, K.V., COUSTENIS, A., DROUIN, B.J., FLAUD, J.-M., GAMACHE, R.R., HODGES, J.T., JACQUEMART, D., MLAWER, E.J., NIKITIN, A.V., PEREVALOV, V.I., ROTGER, M., TENNYSON, J., TOON, G.C., TRAN, H., TYUTEREV, V.G., ADKINS, E.M., BAKER, A., BARBE, A., CANÉ, E., CSÁSZÁR, A.G., DUDARYONOK, A., EGOROV, O., FLEISHER, A.J., FLEURBAEY, H., FOLTYNOWICZ, A., FURTENBACHER, T., HARRISON, J.J., HARTMANN, J.-M., HORNEMAN, V.-M., HUANG, X., KARMAN, T., KARNIS, J., KASSI, S., KLEINER, I., KOFMAN, V., KWABIA-TCHANA, F., LAVRENTIEVA, N.N., LEE, T.J., LONG, D.A., LUKASHEVSKAYA, A.A., LYULIN, O.M., MAKHNEV, V.Y., MATT, W., MASSIE, S.T., MELOSSO, M., MIKHAIL. HARTMANN, J.-M., 2009, A simple empirical model for the collisional spectral shift of air-broadened CO<sub>2</sub> lines, **Journal of Quantitative Spectroscopy and Radiative Transfer**, Volume 110, pages 2019-2026.

[14] HASHEMI, R., GORDON, I.E., TRAN, H., KOCHANOV, R.V., KARLOVETS, E.V., TAN, Y., LAMOUREUX, J., NGO, N.H., ROTHMAN, L.S., 2020, Revising the line-shape parameters for air- and self-broadened CO<sub>2</sub> lines toward a sub-percent accuracy level, **Journal of Quantitative Spectroscopy and Radiative Transfer**, Volume 256, pages 107283.

[15] HASHEMI, R., GORDON, I.E., TRAN, H., KOCHANOV, R.V., KARLOVETS, E.V., TAN, Y., LAMOUREUX, J., NGO, N.H., ROTHMAN, L.S., 2020, Revising the line-shape parameters for air- and self-broadened CO<sub>2</sub> lines toward a sub-percent accuracy level, **Journal of Quantitative Spectroscopy and Radiative Transfer**, Volume 256, pages 107283.

[16] ZAK, E., TENNYSON, J., POLYANSKY, O.L., LODI, L., ZOBOV, N.F., TASHKUN, S.A., PEREVALOV, V.I., 2016, A room temperature CO<sub>2</sub> line list with ab initio computed intensities, **Journal of Quantitative Spectroscopy and Radiative Transfer**, Volume 177, pages 31-42.

[17] TASHKUN, S.A., PEREVALOV, V.I., GAMACHE, R.R., LAMOUREUX, J., 2019, CDSD-296, high resolution carbon dioxide spectroscopic databank: An update, **Journal of Quantitative Spectroscopy and Radiative Transfer**, Volume 228, pages 124-131.

[18] TROKHIMOVSKIY, A., PEREVALOV, V., KORABLEV, O., FEDOROVA, A.A., OLSEN, K.S., BERTAUX, J., PATRAKEEV, A., SHAKUN, A., MONTMESSIN, F., LEFÈVRE, F., LUKASHEVSKAYA, A., 2020, First observation of the magnetic dipole CO<sub>2</sub> absorption band at 3.3 μm in the atmosphere of Mars by the ExoMars Trace Gas Orbiter ACS instrument, **Astronomy & Astrophysics**, Volume 639, pages A142.

[19] ZAK, E., TENNYSON, J., POLYANSKY, O.L., LODI, L., ZOBOV, N.F., TASHKUN, S.A., PEREVALOV, V.I., 2016, A room temperature CO<sub>2</sub> line list with ab initio computed intensities, **Journal of Quantitative Spectroscopy and Radiative Transfer**, Volume 177, pages 31-42.

[20] TASHKUN, S.A., PEREVALOV, V.I., GAMACHE, R.R., LAMOUREUX, J., 2015, CDSD-296, high resolution carbon dioxide spectroscopic databank: Version for atmospheric applications, **Journal of Quantitative Spectroscopy and Radiative Transfer**, Volume 152, pages 45-73.

[21] TASHKUN, S.A., PEREVALOV, V.I., GAMACHE, R.R., LAMOUREUX, J., 2019, CDSD-296, high resolution carbon dioxide spectroscopic databank: An update, **Journal of Quantitative Spectroscopy and Radiative Transfer**, Volume 228, pages 124-131.

- [22] BORKOV, Y., SOLODOV, A., SOLODOV, A., PEREVALOV, V., 2021, Line intensities of the 01111-00001 magnetic dipole absorption band of  $^{12}\text{C}^{16}\text{O}_2$ : Laboratory measurements, **Journal of Molecular Spectroscopy**, Volume 376, page 111418.
- [23] KARLOVETS, E.V., GORDON, I.E., ROTHMAN, L.S., HASHEMI, R., HARGREAVES, R.J., TOON, G.C., CAMPARGUE, A., PEREVALOV, V.I., ČERMÁK, P., BIRK, M., WAGNER, G., HODGES, J.T., TENNYSON, J., YURCHENKO, S.N., 2021, The update of the line positions and intensities in the line list of carbon dioxide for the HITRAN2020 spectroscopic database, **Journal of Quantitative Spectroscopy and Radiative Transfer**, Volume 276, page 107896.
- [24] PREDIO-CROSS, A., UNNI, A., LIU, W., SCHOFIELD, I., HOLLADAY, C., MCKELLAR, A., HURTMANS, D., 2007, Line shape parameters measurement and computations for self-broadened carbon dioxide transitions in the 30012  $\leftarrow$  00001 and 30013  $\leftarrow$  00001 bands, line mixing, and speed dependence, **Journal of Molecular Spectroscopy**, Volume 245, pages 34-51.
- [25] HASHEMI, R., ROZARIO, H., IBRAHIM, A., PREDIO-CROSS, A., 2013, Line shape study of the carbon dioxide laser band I, **Canadian Journal of Physics**, Volume 91, pages 924-936.
- [26] BIRK, M., RÖSKE, C., WAGNER, G., 2021, High accuracy  $\text{CO}_2$  Fourier transform measurements in the range 6000–7000  $\text{cm}^{-1}$ , **Journal of Quantitative Spectroscopy and Radiative Transfer**, Volume unknown, page 107791.
- [27] TAN, Y., SKINNER, F.M., SAMUELS, S., HARGREAVES, R.J., HASHEMI, R., GORDON, I.E., 2022,  $\text{H}_2$ , He, and  $\text{CO}_2$  line-broadening coefficients, and temperature-dependence exponents for the HITRAN database. Part II:  $\text{CO}_2$ ,  $\text{N}_2\text{O}$ , CO,  $\text{SO}_2$ , OH, OCS,  $\text{H}_2\text{CO}$ , HCN,  $\text{PH}_3$ ,  $\text{H}_2\text{S}$  and  $\text{GeH}_4$ , **Astrophysical Journal Supplement Series**, Volume 262, page 40.
- [28] MISHRA, A. K., SCHIAVON, S., WARGOCKI, P., THAM K. W., 2021, *Respiratory performance of humans exposed to moderate levels of carbon dioxide*. **Indoor Air**, Vol. 31.